Organic Electronics 13 (2012) 1356–1364

Contents lists available at SciVerse ScienceDirect

Organic Electronics

journal homepage: www.elsevier.com/locate/orgel

Fermi level positioning in organic semiconductor phase mixed composites: The internal interface charge transfer doping model

Thomas Mayer [a,*], Corinna Hein [a], Eric Mankel [a], Wolfram Jaegermann [a,c], Mathis M. Müller [b], Hans-Joachim Kleebe [b]

[a] Materials Science Institute, Technische Universität Darmstadt, Petersenstraße 32, D-64287 Darmstadt, Germany
[b] Geo Science Institute, Technische Universität Darmstadt, Schnittspahnstraße 9, D-64287 Darmstadt, Germany
[c] Center of Smart Interfaces, Technische Universität Darmstadt, Petersenstraße 32, D-64287 Darmstadt, Germany

ARTICLE INFO

Article history:
Received 12 December 2011
Received in revised form 14 March 2012
Accepted 18 March 2012
Available online 8 April 2012

Keywords:
Phase mixed organic–organic semiconductors
Phase mixed inorganic–organic semiconductors
Internal interface charge transfer doping

ABSTRACT

Photoemission data, taken on co-sublimed films and on bilayers of the prototypical small molecule semiconductor CuPc and p-type dopants TCNQ or WO_3 show similar electronic trends that have to be interpreted by phase separation of the dopant within the matrix material forming a phase mixed composite. High resolution TEM micrographs for CuPc:WO_3 co-deposited films clearly prove such phase separation. Therefore the doping models developed for singly dispersed dopant molecules cannot be applied. For the mechanism of the doping induced variations of the host matrix Fermi level in such phase mixed semiconductor:dopant composites we propose the internal interface charge transfer doping model. According to this model the Fermi levels of two mixed phases align at the internal interfaces and the doping limit is defined by the work function difference of matrix and dopant minus the potential drops induced by dipole formation at the internal matrix/dopant interfaces. It is shown that the magnitude of the internal interface dipole potential drops may be estimated from the dipoles measured at matrix/dopant bilayer interfaces and that the maximum dopant induced Fermi level shift may be estimated from the difference of work functions measured on thick films of matrix and of dopant, minus a mean value for the interface dipole.

1. Introduction

One of the basic parameters for the discussion of organic electronics is the thermodynamic equilibrium position of the electron electrochemical potential, the so-called Fermi level, which is shifted from a mid gap position towards the LUMO conduction band by n-doping or towards the HOMO valance band by p-doping. Doping of semiconductors is a prerequisite to reach sufficient conductivity and to engineer built-in electric fields at hetero junction interfaces [1–3]. While in inorganic semiconductors the dopant concentration is in the range of ppm, in organic semiconductors concentrations in the range of a few to tens of percent are common [1]. In organic semiconductors doping does not only increase charge carrier concentration but also their mobility as deep traps, which slow down hopping mobility become occupied [4]. Doping is also important for designing space charge layers supporting charge carrier separation at exciton splitting donor/acceptor interfaces in organic solar cells [5]. We have shown that at such interfaces detrimental fields may exist, which oppose charge diffusion from the interface to the electrodes as for intrinsic materials the work function Φ of the electron donor is in general smaller than Φ of the electron acceptor. In addition we have shown that these fields can be reversed to the photovoltaic beneficial

* Corresponding author.
E-mail address: mayerth@surface.tu-darmstadt.de (T. Mayer).

1566-1199/$ - see front matter © 2012 Elsevier B.V. All rights reserved.
http://dx.doi.org/10.1016/j.orgel.2012.03.028

direction by p-doping of the donor [6]. Various concepts of p-type doping of small molecular semiconductors have been presented, e.g. exposure to oxidizing gases such as oxygen or iodine [7–10], co-sublimation of Lewis acids [11], aromatic acceptor molecules [12–14] and transition metal oxides [15–18]. Low doping efficiency for MoO_3 in CBP was found [19] and explained by formation of small MoO_3 clusters that were observed by AFM for MoO_3 deposited onto pentacene [20]. The formation of MoO_3 and ReO_3 precipitates of 0.7–1.4 nm average size within a NPB matrix has recently been observed by TEM for dopant concentrations of 2–25 mol% [21].

In the common doping model for small molecule organic semiconductors matrix and dopant exchange charges between their highest occupied molecular orbital HOMO and lowest unoccupied molecular orbital LUMO states. In the case of p-type doping, a matrix molecule transfers an electron from its HOMO to the energetically favorable LUMO of an acceptor dopant molecule [22], so called integer electron transfer [23] leading to full ionization of the dopant. This model is based on the assumption that single dopant molecules are dissolved in the matrix semiconductor [24] and that the p-dopant LUMO is energetically lined up below the matrix HOMO. Also for p-doping with metal oxides, it was assumed that molecular entities as Mo_3O_9 clusters exchange charge with the organic matrix [18]. Low doping efficiency was assumed to be due to formation of clusters of dopant molecules that are ionized in part only [20,21]. In this publication we give additional evidence that the assumption of single dispersed molecules is not valid in general and for the metal oxide WO_3 clear evidence is given for precipitate formation in CuPc at higher doping concentrations. We show that the matrix Fermi level is shifted in the p doping direction although the acceptor precipitate LUMO band or metal oxide conduction band minimum is lined up above the matrix HOMO band. Evidence is given using photoelectron spectroscopy, that for such phase mixed composites of dopant precipitates embedded in a matrix, charge exchange is governed by thermodynamic Fermi level equalization at internal interfaces of matrix and dopant. The charges transferred from matrix to dopant, inducing the shift of the Fermi level due to space charge in the matrix phase, may reside on dopant surface states at the internal interface similar to surface transfer doping [25–27] or in space charge regions in the dopant precipitates. Thus at the internal interfaces the dopant phase Fermi level may be pinned to the dopant surface states or it may shift in opposite direction to the doping induced Fermi level shift in the matrix phase.

Photoelectron spectroscopy is a well established method to derive basic electronic parameters of inorganic semiconductors and semiconductor interfaces, which can be applied to organic semiconductors as well [28].

2. Experimental

Thin films were produced by thermal evaporation of powders from home made effusion cells. CuPc provided by BASF SE was cleaned three times by gradient sublimation. WO_3 with a purity of 99.9% was purchased by Sigma Aldrich. As substrates commercial 120 nm ITO on glass from Merck KGaA was used. Preparation and synchrotron induced photoemission spectroscopy was performed at the integrated system SoLiAs (Solid Liquid Analysis System) [29] at the U49/2-PGM2 beamline at the synchrotron light source BESSY II in Berlin. The analyzed area is given by the elliptical synchrotron light spot of 200 by 300 μm. The base pressure of the system is 10^{-10} mbar. The system is equipped with a SPECS Phoibos 150 hemispherical analyzer. In the used range from 90 to 600 eV excitation energy an overall resolution of 200–240 meV is reached. The photoelectron kinetic energy given by orbital binding energy and chosen photon energy defines the photo electron mean free path of 0.6–1.7 nm. For the measurement of secondary electron edges a 6 eV negative bias voltage was applied. All binding energies are given with respect to the Fermi level of a metallic reference sample. All spectral features of the valence band and core level regions have been measured and are equivalent to published data.

A series of CuPc:WO_3 composites was produced by co-evaporation of CuPc and WO_3 controlling the ratio of the two materials by source temperature variations. For each composite a new substrate was used. The WO_3 content was deduced from core level photoemission intensity of matrix and dopant phase in the composites as compared to the intensity in the not intentionally doped materials. For the interface experiment WO_3 was stepwise deposited onto an approximately 30 nm thick CuPc layer. The deposition time was doubled each step, beginning with 2 s until the substrate emission lines could not be detected any more and no further changes in the binding energy positions occurred. The adsorbed film thickness was determined from damping of the substrate emission. To test commutativity, CuPc was deposited similarly onto a WO_3 film. A similar procedure was applied for the CuPc:TCNQ composites and the TCNQ/CuPc interface measurements. The standard CuPc, TCNQ and WO_3 source temperatures were 365, 120, and 1000 °C as measured by a thermocouple attached to the crucible. All deposition processes were performed with the substrate at room temperature without active temperature control. During CuPc deposition the sample temperature increased to 40 °C. Using the WO_3 source, a respective higher increase has to be expected.

TEM samples were prepared by co-sublimation of CuPc matrix and WO_3 dopant on thin silicon oxide grids using the same conditions as for composites for SXPS analysis. Again the ratio between CuPc and WO_3 was controlled by the source temperatures. Composite thickness was determined by source calibration using damping of substrate photoemission lines. The layer thickness of the TEM sample was approximately 30 nm.

High-resolution transmission electron microscopy (HRTEM) was performed using a FEI CM20 instrument (FEI, Eindhoven, The Netherlands) operating at 200 kV. TEM samples were prepared by directly depositing the thin film onto a copper grid coated with a 15 nm thin amorphous silica support in order to avoid any artefacts upon standard sample preparation techniques. Light carbon coating was utilized to minimize charging under the incident electron beam.

3. Results and discussion

We measured valence states and core orbital photoelectron spectra of CuPc and TCNQ films, of CuPc:TCNQ co-evaporated films, and of TCNQ/CuPc interfaces [30]. The particular films were deposited up to a thickness that showed the respective work function and Fermi level position free of influences by the respective substrate. The work function of an organic film derived from the valence band photoemission spectra cut off may depend on the substrate work function due to charge exchange between substrate and organic semiconductor at the interface [23,31]. Film thicknesses that show the work function free of influences of the interface to the substrate depend on mobile charge carrier concentration due to intentional or unintentional doping by e.g. impurities and background gas incorporation. For highly intrinsic C60 e.g. 500 nm were needed to measure by Kelvin probe a common, substrate independent, work function [32]. In the case of CuPc we needed around 30–40 nm.

Spectra of the mixed composite film and of CuPc on TCNQ were shown to be a superposition of the spectra of the single materials, indicating the absence of a chemical reaction. It was also shown in [30] that the growth mode of CuPc on TCNQ changes from monolayer to island growth indicated by a pronounced change of the slope of the logarithmic HOMO intensity increase with deposition time at 0.7 nm CuPc thickness. This was interpreted as a change from growth of a monolayer to island growth on top.

In Fig. 1 the deduced band diagrams are compared. Two energy gaps are considered for CuPc in Fig. 1(c). The UPS HOMO and LUMO onset gap of 1.7 eV that is close to the optical absorption gap [33], and the UPS HOMO and LUMO maximum gap of 3.1 eV [34]. As small binding energy shifts are more clearly identified from maxima, we communicate these positions, although nowadays onset values additionally given in Fig. 1 are more common in publications. In order to position the TCNQ LUMO orbital we use the UPS/IPS gap between the HOMO and LUMO maxima of F_4-TCNQ that has been determined to be 4.35 eV [35]. In general orbital energies of small organic molecules vary strongly with substitution while the HOMO–LUMO gap is influenced only weakly as shown e.g. for F_xZnPc in [36]. With these values the energy position of the TCNQ LUMO maximum is found 4.23 eV below the vacuum level well above the CuPc HOMO maximum at 5.66 eV, while the TCNQ Fermi level is found 790 meV below the CuPc Fermi level although TCNQ shows strong unintentional n- and CuPc weak unintentional p-doping. Thus considering relative orbital positions in the vacuum level line up in Fig. 1(a) and (b), electron transfer from CuPc to TCNQ is not expected, while thermodynamic equalization of the Fermi levels at the interface requires electron transfer from the CuPc phase to the TCNQ phase.

With increasing TCNQ content the emissions of the CuPc valence and core levels shift to lower binding energy. As in photoemission, binding energies are referenced to the Fermi level, the induced shifts indicate p-doping. 0.2 eV maximal binding energy shifts of MeO-TPD core and valence orbital emissions induced by F_4-TCNQ doping have been shown to correspond to increased conductivity by three orders of magnitude [22]. TCNQ shows an initial doping efficiency of 21 meV/mol% and a saturation value of 400 meV reached at about 80% dopant content. At the TCNQ/CuPc interface 390 meV of the work function difference are compensated by band bending in the CuPc film of $eV_{bb}^{M} = 350$ meV and in the TCNQ layer of $eV_{bb}^{D} = 40$ meV. The missing 400 meV to fully compensate the work function difference are assigned to an interface dipole potential. In general in the interface dipole several effects are summed up, as e.g. changes of the substrate surface dipole induced by the adsorbate, often called the "push back" effect, possible partial charge transfer in heteropolar interface bonding interaction, and the difference of the

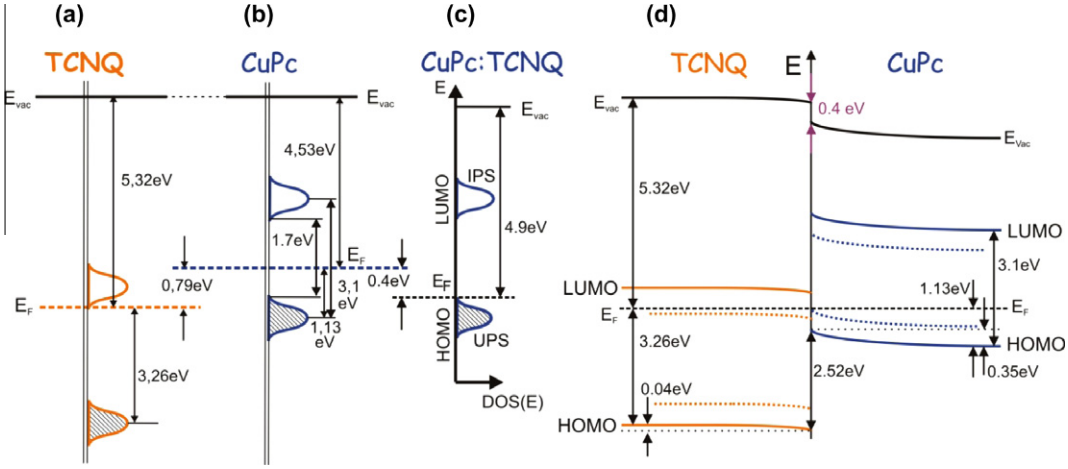

Fig. 1. Band energy diagrams of (a) TCNQ thick film, (b) CuPc thick film, (c) CuPc:TCNQ mixed layer with high TCNQ content, and (d) TCNQ/CuPc bilayer. Aligning the vacuum levels (a) and (b) the work function difference shows the CuPc Fermi level 790 meV above the TCNQ Fermi level. TCNQ induced Fermi level shift in CuPc (b) and (c). After contact formation an interface dipole potential drop of 400 meV and band bending towards the interface of 40 meV down in TCNQ and 350 meV up in CuPc are induced to compensate the work function difference. Dotted lines in (d) indicate HOMO and LUMO onsets in addition to the maxima positions.

adsorbed layer surface dipole towards the interface versus the dipole of the free surface, on which the work function of the adsorbed film is measured [37].

The comparable values of the maximum band bending in TCNQ/CuPc bilayers and the shift of the Fermi level in the CuPc:TCNQ co-sublimed films motivates to correlate the Fermi level shift at the interface with the Fermi level movement induced by CuPc:TCNQ doping. Postulating TCNQ dopant precipitates within the CuPc host matrix that comprise mobile charges carriers, which occupy the density of states according to Fermi distribution with a defined Fermi level, Fermi level equalization of the two materials is achieved in the composite by formation of dipole potential drops at the internal interfaces and by charge transfer leading to internal space charge regions. For such mixed phases we propose the internal interface charge transfer doping model as sketched in Fig. 2. In Fig. 2(a) the spatial distribution of the phases and charges and in Fig. 2(b) the corresponding energy diagram is sketched. For clarity, the dipole potential formation at the internal matrix/precipitate interfaces has been separated from Fermi level movements due to charge transfer. In Fig. 2(a) the structure has been simplified heavily. As shown for WO_3 below, the dopant precipitates may be interconnected and form large enough clusters to bear a defined Fermi level in the dopant precipitate phase. For simplicity in Fig. 2(b) band bending has been neglected, which holds only for small characteristic dimensions in the composites as compared to the extension of space charge regions induced by Fermi level equalization. A single value for the interface dipole potential has been used in the sketch, while in the real composite for different surfaces and morphologies different dipoles will be formed as discussed for WO_3 below. Also neglected is the possible presence of dopant surface/interface states that are well known for the transition metal oxides, to which the dopant Fermi level may be pinned. With increasing dopant content the Fermi level shift ΔE_F^D in the dopant is assumed to become smaller due to the increasing number of available non occupied dopant states and the shift ΔE_F^M in the matrix becomes accordingly stronger. The sketched orbital positions and work functions are drawn in a general manner not scaled to the experimental values of the measured examples. Band bending and possible presence of surface gap states leading to Fermi level pinning are ignored for simplicity.

In the most simplified model situation sketched in Fig. 2, where a single value for δ is considered Eq. (1) holds:

$$\Delta E_F^M = \Delta\Phi - \delta - \Delta E_F^D \quad (1)$$

If it is further assumed that the dipole potential drop at the internal interfaces is of the same value as measured for a bilayer, the maximum Fermi level variations of matrix and dopant ΔE_F^M and ΔE_F^D in the model composite are equal to the maximum band bending eV_{bb} at the matrix/dopant bilayer interface measured on thick enough films that show respective Fermi level position free of respective substrate influences:

$$\Delta E_F^M = eV_{bb}^M \quad (2)$$

$$\Delta E_F^D = eV_{bb}^D \quad (3)$$

With the considered simplifications and the assumptions (2) and (3), all values of Eq. (1) can be determined from matrix/dopant bilayer experiments. Applying the values derived from the CuPc/TCNQ interface experiment to the phase mixed composite, the work function difference $\Delta\Phi$ of 790 meV of the not intentionally doped single materials should be compensated in the phase mixed composite by an interface dipole potential drop δ in the range of 400 meV and Fermi level movements ΔE_F^M of 350 meV downward in the CuPc matrix and ΔE_F^D of 40 meV upward in the TCNQ precipitates. In a real composite, however, a number of different dipole potential values have to be considered due to crystallographic or morphologically different matrix/precipitate interfaces and Eqs. (1)–(3) will hold only approximately. Different dipole potential drops and/or residuary band bending in CuPc may be the cause

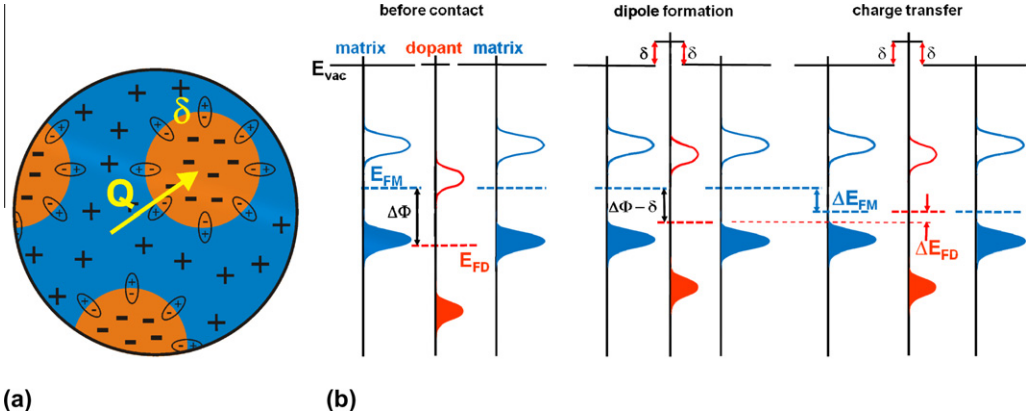

Fig. 2. The internal interface charge transfer doping model. The work function difference between the matrix material (blue) and the dopant precipitates (orange) is compensated by the formation of an interface dipole potential δ and charge transfer Q between the two phases, which leads to Fermi level movements ΔE_F^M in the matrix and ΔE_F^D in the dopant phase. E_{FM} and E_{FD} are thick layer Fermi level positions, free of substrate influences. (a) spatial model and (b) development of the corresponding band energy diagram separating dipole formation and thermodynamic Fermi level equalization. (For interpretation of the references to colour in this figure legend, the reader is referred to the web version of this article.)

of the experimentally observed broadening of the CuPc photoemission lines in the CuPc/TCNQ composites versus the not intentionally doped CuPc film by about 0.3 eV (FWHM). In practical doping experiments an effective doping limit will be reached that may deviate from the maximum band bending observed in a specific matrix/dopant interface experiment.

As an attempt to explicitly correlate the electronic structure measured with photoelectron spectroscopy with the proposed morphology of an organic-semiconductor:dopant system, we have investigated the inorganic dopant WO_3 in CuPc, expecting clear contrast in TEM. Again we compare the electronic structure of co-deposites and interfaces. In the photoemission measurements the pure CuPc films showed a more intrinsic position of the Fermi level near mid gap, which corresponds to a smaller work function of 4.1 eV as compared to 4.5 eV in the TCNQ experiments above, which may be due to some TCNQ contamination of the not intentionally doped CuPc film. The band gap of WO_3 prepared in a vacuum PVD process depends on substrate temperature at which deposition was performed [38]. At room temperature the gap is 3.3 eV related to amorphous WO_3 [38,39], which may contain crystalline precipitates [40]. Due to oxygen deficiency vacuum deposited films show gap states, with high surface concentration [41].

Synchrotron induced photoelectron spectra of the valence band, the secondary onset (not displayed) as well as the CuPc and WO_3 core levels have been measured for the three experiments CuPc:WO_3 co-deposition, stepwise PVD of WO_3 onto a thick CuPc substrate for the CuPc/WO_3 interface and stepwise PVD of CuPc onto a WO_3 substrate for the WO_3/CuPc interface. For both interface sequences we observe a work function change by 2.5 eV indicated by the shift of the secondary electron emission edge.

The valence band spectra measured at 90 eV excitation energy for co-deposited films and the CuPc/WO_3 and WO_3/CuPc interface experiments are displayed in Fig. 3(a)–(c). The bottom spectra in Fig. 3(a) and (b) correspond to pure CuPc and in (c) to pure WO_3. The top spectra in Fig. 3(a) and (b) correspond to pure WO_3 and a thick layer of WO_3 on the CuPc substrate and in Fig. 3(c) to a thick layer of CuPc on the WO_3 substrate. The intermediate spectra correspond to a linear superposition of the pure CuPc and WO_3 spectra indicating the absence of chemical reactions. The WO_3 valence band energy maximum and CuPc HOMO emission maximum is indicated in the pure spectra.

Photoelectron spectra of the CuPc C1s core levels measured for co-deposited films and the CuPc/WO_3 and WO_3/CuPc interface experiments are displayed in Fig. 4(a)–(c). The three C1s maxima are attributed for increasing binding energy, to the aromatic and the pyrrole carbon and a π–π^* shake up satellite of the latter, while the satellite of the aromatic emission is buried under the pyrrole emission [42]. Besides broadening, the line shape of the SXPS C1s emission does not change with WO_3 content indicating the absence of a chemical modification of CuPc due to WO_3 co-deposition. Also the PVD of WO_3 onto CuPc does not alter the C1s line shape indicating chemical stability. In Fig. 4(a) p-doping is evident by a shift to lower binding energy. A maximum shift of 0.69 eV is reached at 55 mol% WO_3. The corresponding photoemission spectra of the CuPc/WO_3 and WO_3/CuPc interface experiments Fig. 4(b) and (c) show binding energy shifts of 0.5 and 1.0 eV, which correspond to band bending. Subtracting band bending and shifts of zero and 80 meV of the Fermi level in WO_3, from the work function change, results in induced interface dipoles of 2.0 and 1.42 eV in the two adsorption sequences. Similarly strong dipole potentials have recently been measured at the interface between WO_3 and the hole transport layer TCTA [43]. The valence band and core level spectra

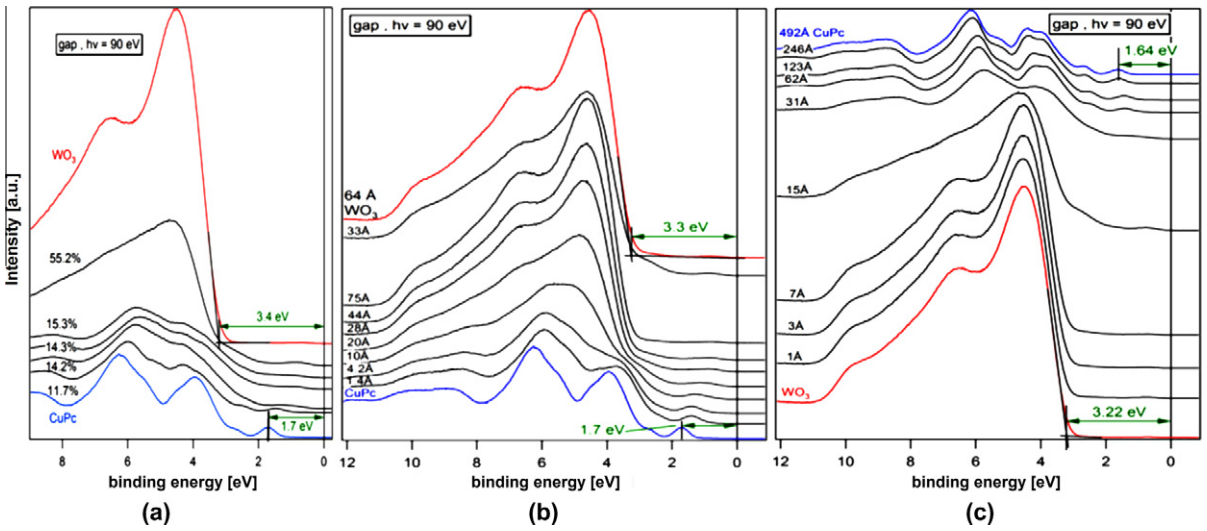

Fig. 3. Synchrotron induced valence band spectra at $h\nu$ = 90 eV excitation energy of (a) CuPc:WO_3 composites with indicated WO_3 content from pure CuPc (bottom) to pure WO_3 (top), (b) CuPc/WO_3 interface with indicated WO_3 thickness from pure CuPc (bottom) to a thick layer of WO_3(top), and (c) WO_3/CuPc interface from pure WO_3 (bottom) to a thick layer of CuPc (top). The WO_3 valence band energetic maximum and CuPc HOMO emission maximum positions are indicated.

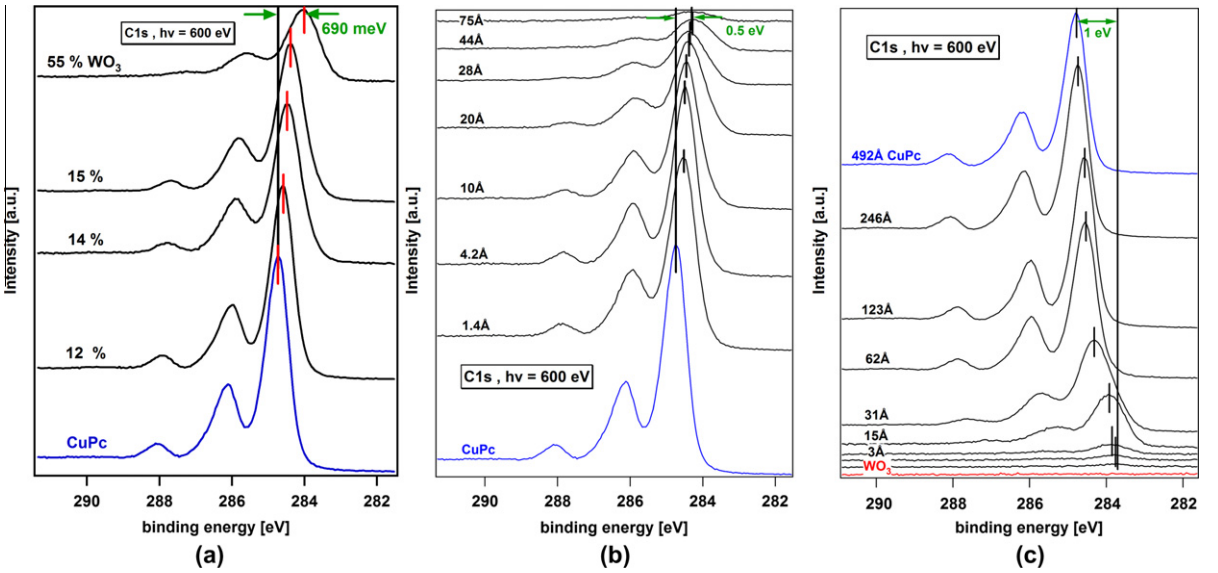

Fig. 4. Synchrotron induced C1s core level spectra at $h\nu$ = 600 eV excitation energy of (a) CuPc:WO_3 composites with indicated WO_3 content, (b) CuPc/WO_3 interface with indicated WO_3 thickness, and (c) WO_3/CuPc interface with indicated CuPc thickness. In (a) p-doping of 0.69 eV, in (b) CuPc band bending of 0.5 eV and in (c) CuPc band bending of 1 eV are indicated.

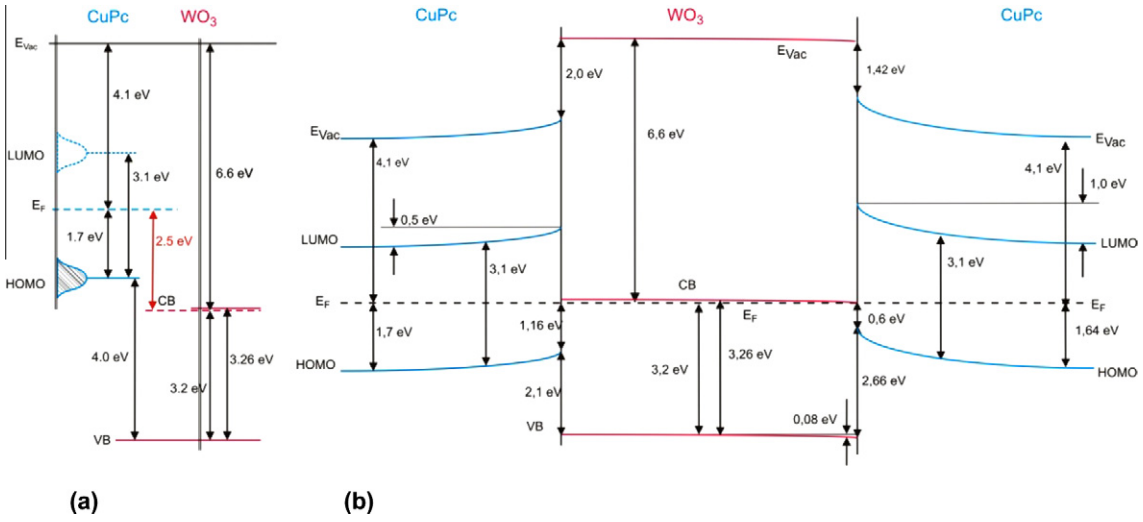

Fig. 5. Band diagram of (a) a thick layer of not intentionally doped CuPc and WO_3 in the vacuum level line up showing a work function difference of 2.5 eV, (b) the two interfaces CuPc/WO_3 and WO_3/CuPc. The work function is compensated by interface dipole potentials of 2.0 and 1.42 eV and band bending of 0.5 and 1.0 eV. The width of the space charge region is around 35 nm as estimated from the WO_3/CuPc experiment. Values are given with respect to the HOMO an LUMO maximum.

can be summarized in the band diagram (Fig. 5). In Fig. 5(a) the band diagrams of the non intentionally doped CuPc and a WO_3 film are compared in the vacuum level line up, showing a work function difference of 2.5 eV. Thus, ignoring interface dipole contributions the CuPc HOMO is positioned above the WO_3 conduction band, suggesting charge transfer from the occupied CuPc HOMO to the empty WO_3 conduction band states. But strong induced interface dipoles of 2.0 and 1.4 eV shift the WO_3 conduction band substantially above the CuPc HOMO as derived from the interface experiments in both adsorption sequences (Fig. 5(b)). Thus at the interfaces the charge transfer is clearly driven by the thermodynamic equalization of the Fermi levels and limited by the work function difference of 2.5 eV minus the interface dipole potential drops of 2.0 and 1.42 eV indicated by band bending of 0.5 and 1.0 eV. Thus, commutativity is not given for the prepared interfaces of CuPc and WO_3, which may be expected as the conditions of WO_3/CuPc are different compared to CuPc/WO_3 considering e.g. the source temperature influencing the substrate temperature. The orientation of the organic molecules and thereby the induced dipole right at the interface

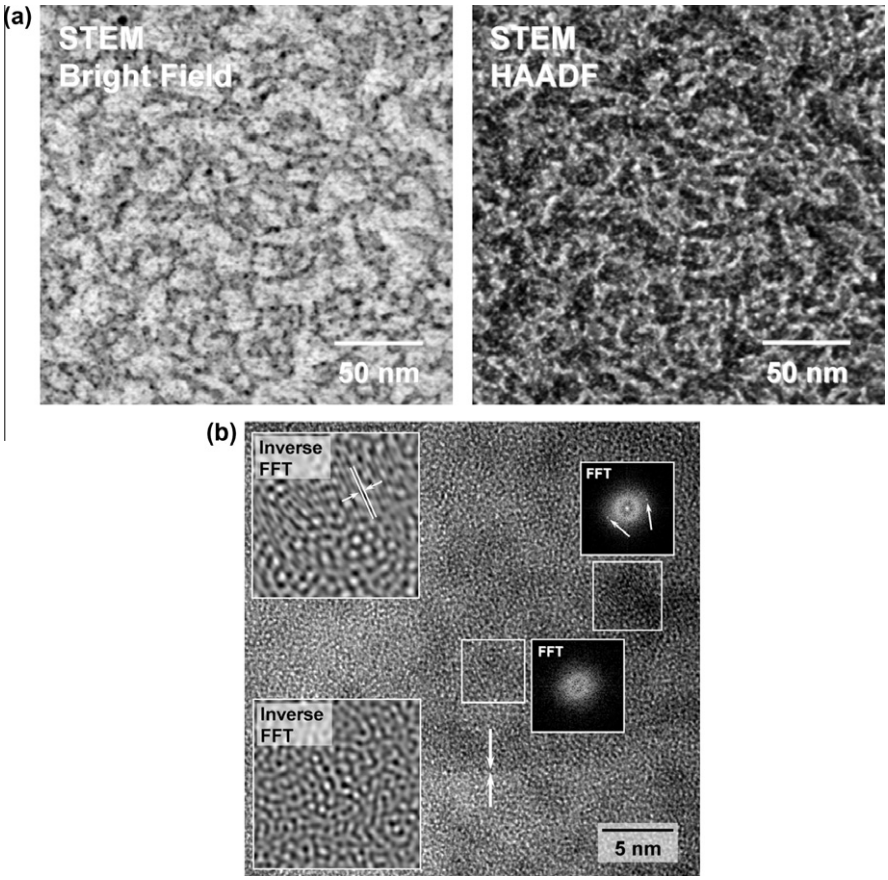

Fig. 6. Morphology of a CuPc:WO_3 composite containing 30 mol% WO_3. (a) In the scanning TEM images local precipitations of WO_3 in nm size and distance appear as dark features in BF and bright features in HAADF mode as identified by energy dispersive spectroscopy EDS. The images were taken with a spot size of 5 Å. (b) In high-resolution TEM image the dark areas indicate tungsten oxide. Insets show both local electron diffraction FFT and high resolution inverse FFT (at a higher magnification) of the area indicated by white squares. The upper area shows distinct diffraction spots in FFT and lattice fringes in Inverse FFT. The lower area shows a diffuse halo in FFT and an amorphous pattern in Inverse FFT. The area in the top square therefore depicts a crystalline WO_3 precipitate, while the area in the lower square corresponds to an amorphous WO_3 phase. Note that also the interface between the amorphous WO_3 phase and CuPc, indicated by white arrows, is rather sharp. The sample contains 30 mol% of tungsten oxide.

may differ [44,45] in the two deposition sequences due to increased mobility of CuPc molecules when deposited onto WO_3 compared to the already formed film on which WO_3 is deposited.

As the deposition rate of the CuPc source has been determined, the width of the space charge layer can be estimated to be 35 nm. Due to a high concentration of gap states on the WO_3 surface the Fermi level is pinned and no space charge region is formed in WO_3.

As in the TCNQ doping case, we correlate the Fermi level variation in the CuPc:WO_3 composites with the band bending at the bilayer interfaces. The value of the maximum Fermi level movement in the WO_3 doped CuPc films of 690 meV is in-between the values of the band bending at the CuPc/WO_3 (500 meV) and the WO_3/CuPc (1 eV) interfaces. The Fermi level variation is explained by the interface charge transfer doping model: the work function difference between CuPc of $\Phi = 4.1$ eV and WO_3 of $\Phi = 6.6$ eV is compensated in part by the formation of dipole potential drops at the internal interfaces between CuPc and WO_3 in the range of 1.42–2 eV and an effective Fermi level movement of up to $\Delta E_F^M = 690$ meV. Due to Fermi level pinning at WO_3 gap states, ΔE_F^D is very small (below 80 meV) as compared to the TCNQ case.

In order to verify the formation of dopant precipitates at higher dopant concentrations, scanning and high-resolution transmission electron microscopy (STEM and HRTEM) imaging was performed on CuPc:WO_3 samples. The same PVD evaporation conditions in UHV of 10^{-9} mbar were applied, as used for the photoemission experiments mentioned above. Due to the high atomic number of W, a contrast in transmission electron microscopy between CuPc and WO_3 is expected. Scanning TEM images, taken in bright field (BF) and high angle annular dark field (HAADF) mode, of a CuPc:WO_3 sample containing 30% WO_3 are shown in Fig. 6(a). Due to the high atomic number of tungsten, WO_3 precipitates appear dark in BF mode versus CuPc (Fig. 6(a) left), while the contrast is reversed in HAADF mode (Fig 6(a) right). The spot size used for those measurements was 5 Å. There are spot like dark/bright (BF/HAADF) regions surrounded partly by less dark/bright more diffuse areas. Energy dispersive spectroscopy (EDS)

analysis revealed a high tungsten signal in dark BF regions, which clearly identifies the dark BF regions as WO_3 precipitates. Similar precipitation has been found recently in HRTEM images of of MoO_3 and ReO_3 in the organic semiconductor NPB [21]. A HRTEM image together with local Fast Fourier Transformation FFT and Inverse FFT analysis are shown in Fig. 6(b). W containing phases appear dark in HRTEM. The local diffraction patterns in FFT and the corresponding high resolution image in inverse FFT of two areas are shown in the insets of Fig. 6(b). While the upper area shows distinct diffraction spots in FFT and the Inverse FFT clearly reveals lattice fringes, the lower area shows a diffuse halo in FFT and an amorphous pattern in Inverse FFT. Therefore, it is concluded that the dark/bright spots in Fig. 6(a) and (b) are nanosized crystalline WO_3 precipitates, while the areas in close proximity consist of amorphous tungsten oxide. The interface between CuPc and the amorphous WO_3 phase is rather sharp allowing for the formation of distinct interface dipole layers also here. The small extension of the CuPc matrix interspaces of around 2 nm as compared to the space charge region in the CuPc/WO_3 bilayer case of around 35 nm leads to the semi quantitative coincidence of the maximum band bending in the bilayer and the maximum Fermi level variation in the composites.

Thus, while at low dopant concentrations transition metal oxide molecules or small clusters have been shown to be present in the organic matrix (e.g. for MoO_3 doped pentacene [20]), it is shown here by HRTEM that at higher dopant concentrations dopant and matrix form phase mixed composites.

4. Conclusion

For the organic/inorganic doping case CuPc:WO_3 the formation of WO_3 precipitates at higher dopant concentrations has clearly been revealed by STEM, proving the conclusions drawn on phase mixed morphology from photoemission measurements on CuPc:WO_3 composites and CuPc/WO_3 and WO_3/CuPc interfaces. Hence the morphological preconditions for application of the internal interface charge transfer doping model are evidently given for the inorganic dopant WO_3 at higher concentrations. As the electronic behavior is similar for the inorganic and organic dopant case, we feel safe to conclude that also the organic dopant forms precipitates and the internal interface charge transfer doping model holds in the CuPc:TCNQ case at higher concentrations as well. The transition between dispersed dopant molecules that are fully ionized [23] over clusters of in part ionized molecular entities [20] to precipitates with a Fermi distribution of mobile charges to which the internal interface charge transfer doping model applies, may be expected to depend on the matrix and dopant materials, their unintentional doping level due to impurities and imperfections, there combination concerning interface tensions, and certainly their concentration ratio. For specific combinations, the instability of the dopant distribution may also lead to precipitate formation over time. New methods for the mapping of organic:organic composites have to be developed to directly reveal the morphology on the nm scale. For mixed phases of matrix and dopant precipitates that comprise a Fermi distribution of mobile charge carriers, Fermi level equalization of the two materials is achieved in the composite by formation of dipole potential drops at the internal interfaces and by charge transfer leading to internal space charge regions extending throughout the typical matrix dimensions. According to the internal interface charge transfer doping model, the Fermi level in the organic semiconductor matrix is shifted due to thermodynamic equalization with the dopant phase Fermi level. The doping limit is given by the work function difference of matrix and dopant minus the potential drops induced by dipole formation at the internal matrix/dopant interfaces. In the most simple model a single mean value for the dipole potential drop is assumed, while at the CuPc/WO_3 and WO_3/CuPc interfaces substantially different dipole drops have been measured. According to this simple model internal interface charge transfer doping can be correlated with interface experiments. The values needed to propose the dopant induced maximum Fermi level shift can be derived in principal using photoelectron spectroscopy on sequentially deposited matrix/dopant bilayers, each layer thick enough to show the respective Fermi level position undisturbed by the substrate, and using the same material supply and deposition conditions as used for the phase mixed composite. The internal interface charge transfer doping model may also apply to predict Fermi level positioning in other phase mixed systems important in technological applications as e.g. bulk heterojunction solar cells.

Acknowledgments

We would like to acknowledge our cooperation partners Peter Erk and Jaehyung Hwang from BASF. The experiments have been performed within the OPEG project funded by the German Ministry of Education and Research BMBF.

References

[1] M. Pfeiffer, A. Beyer, T. Fritz, K. Leo, Applied Physics Letters 73 (1998) 3202.
[2] W.Y. Gao, A. Kahn, Journal of Physics: Condensed Matter 15 (2003) S2757.
[3] W. Jaegermann, A. Klein, T. Mayer, Advanced Materials 21 (2009) 4196.
[4] B. Maennig, M. Pfeiffer, A. Nollau, X. Zhou, K. Leo, P. Simon, Physical Review B 64 (2001) 195208.
[5] A. Liu, S. Zhao, S.B. Rim, J. Wu, M. Konemann, P. Erk, P. Peumans, Advanced Materials 1065 (2008) 20.
[6] C. Hein, E. Mankel, T. Mayer, W. Jaegermann, Physica Status Solidi A: Applications and Materials Science 206 (2009) 2757.
[7] A. Twarowski, Journal of Chemical Physics 77 (1982) 5840.
[8] T.D. Anthopoulos, T.S. Shafai, Applied Physics Letters 82 (2003) 1628.
[9] T. Nishi, K. Kanai, Y. Ouchi, M.R. Willis, K. Seki, Chemical Physics Letters 414 (2005) 479.
[10] S.F. Chen, Y.K. Fang, S.C. Hou, C.Y. Lin, C.S. Lin, W.R. Chang, T.H. Chou, Organic Electronics 6 (2005) 92.
[11] J. Endo, T. Matsumoto, J. Kido, Japanese Journal of Applied Physics Part 2: Letters 41 (2002) L358.
[12] M. Maitrot, G. Guillaud, B. Boudjema, J.J. Andre, J. Simon, Journal of Applied Physics 60 (1986) 2396.
[13] Z.Q. Gao, B.X. Mi, G.Z. Xu, Y.Q. Wan, M.L. Gong, K.W. Cheah, C.H. Chen, Chemical Communications (2008) 117.
[14] W.Y. Gao, A. Kahn, Applied Physics Letters 79 (2001) 4040.
[15] C.C. Chang, M.T. Hsieh, J.F. Chen, S.W. Hwang, C.H. Chen, Applied Physics Letters 89 (2006) 253504.

[16] D.S. Leem, H.D. Park, J.W. Kang, J.H. Lee, J.W. Kim, J.J. Kim, Applied Physics Letters 91 (2007) 011113.
[17] G.H. Xie, Y.L. Meng, F.M. Wu, C. Tao, D.D. Zhang, M.J. Liu, Q. Xue, W. Chen, Y. Zhao, Applied Physics Letters 92 (2008) 093305.
[18] M. Kroger, S. Hamwi, J. Meyer, T. Riedl, W. Kowalsky, A. Kahn, Organic Electronics 10 (2009) 932.
[19] S. Hamwi, J. Meyer, T. Winkler, T. Riedl, W. Kowalsky, Applied Physics Letters 94 (2009) 253307.
[20] S.D. Ha, J. Meyer, A. Kahn, Physical Review B 82 (2010) 155434.
[21] J.H. Lee, H.M. Kim, K.B. Kim, J.J. Kim, Organic Electronics 12 (2011) 950.
[22] S. Olthof, W. Tress, R. Meerheim, B. Lussem, K. Leo, Journal of Applied Physics (2009) 106.
[23] S. Braun, W.R. Salaneck, M. Fahlman, Advanced Materials 21 (2009) 1450.
[24] S.D. Ha, A. Kahn, Physical Review B 80 (2009) 1098.
[25] P. Strobel, M. Riedel, J. Ristein, L. Ley, Nature 430 (2004) 439.
[26] W. Chen, X.Y. Gao, D.C. Qi, S. Chen, Z.K. Chen, A.T.S. Wee, Advanced Functional Materials 17 (2007) 1339.
[27] M. Irfan, H. Zhang, C.W. Ding, Y. Tang, Gao, Organic Electronics 12 (2011) 1588.
[28] Y. Gao, Materials Science and Engineering Reports 68 (2010) 39.
[29] T. Mayer, M. Lebedev, R. Hunger, W. Jaegermann, Applied Surface Science 252 (2005) 31.
[30] T. Mayer, C. Hein, J. Haerter, E. Mankel, W. Jaegermann, Proceedings of SPIE 7052 (2008) 705204.
[31] C. Tengstedt, W. Osikowicz, W.R. Salaneck, I.D. Parker, C.H. Hsu, M. Fahlman, Applied Physics Letters 88 (2006).
[32] N. Hayashi, H. Ishii, Y. Ouchi, K. Seki, Journal of Applied Physics 92 (2002) 3784.
[33] D.R.T. Zahn, M. Gorgoi, O.D. Gordan, Solar Energy 80 (2006) 707.
[34] I.G. Hill, A. Kahn, Z.G. Soos, R.A. Pascal, Chemical Physics Letters 327 (2000) 181.
[35] W. Gao, A. Kahn, Organic Electronics 3 (2002) 53.
[36] T. Mayer, U. Weiler, C. Kelting, D. Schlettwein, S. Makarov, D. Wöhrle, O. Abdallah, M. Kunst, W. Jaegermann, Solar Energy Materials and Solar Cells 2007 (1873) 91.
[37] W. Jaegermann, The semiconductor/electrolyte interface: a surface science approach, in: Ralph E. White, Brian E. Conway, J. O'M. Bockris (Eds.), Modern Aspects of Electrochemistry, Kluwer Academic/Plenum Publishers, New York, 1996.
[38] K.J. Patel, C.J. Panchal, V.A. Kheraj, M.S. Desai, Materials Chemistry and Physics 114 (2009) 475.
[39] L. Ottaviano, E. Maccallini, S. Santucci, Surface Science 492 (2001) L700.
[40] A. Antonaia, T. Polichetti, M.L. Addonizio, S. Aprea, C. Minarini, A. Rubino, Thin Solid Films 354 (1999) 73.
[41] G.A. de Wijs, R.A. de Groot, Physical Review B 60 (1999) 16463.
[42] L. Ottaviano, S. DiNardo, L. Lozzi, M. Passacantando, P. Picozzi, S. Santucci, Surface Science 373 (1997) 318.
[43] S. Hamwi, J. Meyer, M. Kroeger, T. Winkler, M. Witte, T. Riedl, A. Kahn, W. Kowalsky, Advanced Functional Materials 20 (2010) 1762.
[44] S. Duhm, G. Heimel, I. Salzmann, H. Glowatzki, R.L. Johnson, A. Vollmer, J.P. Rabe, N. Koch, Nature Materials 7 (2008) 326.
[45] T. Mayer, R. Hunger, A. Klein, W. Jaegermann, Physica Status Solidi B: Basic Solid State Physics 2008 (1838) 245.